PHYSICAL REVIEW C **109**, 014313 (2024)

Investigating the prolate-to-oblate shape phase transition: Lifetime measurements and γ spectroscopy of the low-lying negative parity structure in ^{193}Os

L. Knafla,[1,*] K. Nomura,[2] A. Esmaylzadeh,[1] A. Harter,[1] J. Jolie,[1] V. Karayonchev,[1,†] Y. H. Kim,[3,‡] U. Köster,[3]
M. Ley,[1] C. Michelagnoli,[3] A. Pfeil,[1] J.-M. Régis,[1] and F. von Spee[1]
[1]*Institut für Kernphysik, Mathematisch-Naturwissenschaftliche Fakultät, Universität zu Köln, 50937 Köln, Germany*
[2]*Department of Physics, Hokkaido University, Sapporo 060-0810, Japan*
[3]*Institut Laue Langevin, 71 Avenue des Martyrs, 38042 Grenoble, France*

(Received 11 September 2023; accepted 7 December 2023; published 10 January 2024)

Excited states in ^{193}Os were populated using a $^{192}\mathrm{Os}(n_{\mathrm{th.}},\gamma)\,^{193}\mathrm{Os}$ thermal neutron capture reaction, with neutrons provided by the high-flux reactor of the Institut Laue-Langevin in Grenoble, France. Lifetimes of low-spin excited states were measured using the generalized centroid difference method. A total of eight mean lifetimes of low-lying excited states were determined for the first time, and limits for the lifetimes of three further excited states were established. Additionally, γ-γ angular correlations were analyzed to assign spins to previously known excited states up to 1 MeV, and extract multipole mixing ratios for several transitions. The new spectroscopic information is compared to calculations in the framework of the interacting boson-fermion model, based on the nuclear density functional theory, to investigate the prolate-to-oblate shape phase transition, predicted to occur in the neutron rich $A \approx 190$ region.

DOI: 10.1103/PhysRevC.109.014313

I. INTRODUCTION

The neutron rich $A \approx 190$ Pt-Os transitional region is well known for the occurrence of several different nuclear structure phenomena, with prolate, oblate, and triaxial ground state deformations [1–8]. For increasing neutron number the osmium isotopes are predicted to undergo a transition from a dominant prolate to oblate deformation, towards a spherical shape at the $N = 126$ shell closure [1]. The shape phase transition is predicted to occur suddenly between $^{192}\mathrm{Os}_{116}$ and $^{194}\mathrm{Os}_{118}$, with prolate deformation for $N = 116$ and oblate deformation for $N = 118$ [1,4]. Other experimental results in combination with total Routhian surface calculations predict an evolution from a γ-soft prolate minimum at ^{190}Os to a well defined oblate shape at ^{196}Os [9]. In this framework both prolate and oblate γ-soft minima are predicted for ^{194}Os, with the prolate minimum slightly dominating [9]. The comparison of recent spectroscopic data for ^{196}Os to beyond-mean-field calculations, based on the underlying Gogny D1S interaction, suggests a smooth transition in the osmium isotopes through a γ-soft configuration, with triaxial minima for the assumed transitional nuclei ^{190,192}Os, and oblate deformation for $^{194\text{–}198}$Os [10]. Experimental evidence for weakly oblate deformed shape was found for ^{198}Os [2], but the exact details of the structural evolution in the osmium isotopes are not yet comprehensively understood.

The interacting boson model (IBM) calculations by Nomura *et al.*, with the IBM Hamiltonian determined by constrained Hartree-Fock-Bogoliubov (HFB) calculations with the microscopic Gogny-D1M energy density functional, suggest the prolate-to-oblate shape phase transition occurs at $N \approx 116$ [8,11]. The interacting boson-fermion model (IBFM) extension of this approach to odd-A nuclei [12], and the systematic investigation of the prolate-to-oblate shape phase transition in the neutron-rich odd-mass nuclei in the $A \approx 190$ region [13], suggest indicators for shape transitions in the odd-A osmium isotopes. Between ^{191}Os and ^{193}Os the spin of the ground state changes from $9/2^-$ to $3/2^-$, respectively. Further, effective deformation parameters, calculated from quadrupole shape invariants, rapidly change in the range $N = 115$–117, indicating the occurrence of a shape phase transition in these nuclei [13].

Investigating the intermediate odd-A nuclei can help in understanding the transition between the neighboring even-even isotopes. Especially, the theoretical description of the odd-A nucleus ^{193}Os, located at the borders of the expected prolate and oblate deformation, is of relevance to improve the description of the structural evolution in the osmium isotopes. The IBM calculations, based on the Gogny-D1M density functional, predicting the prolate-oblate shape phase transition to occur at $N \approx 116$, are important for the description of the underlying structural behavior. It is of interest to verify, how well the theoretical calculations, are able to describe the odd-A nuclei in the region of shape phase transition.

The available spectroscopic information for ^{193}Os, required to verify the theoretical calculations, is limited: energies of

---

[*] Corresponding author: lknafla@ikp.uni-koeln.de

[†] Present address: Argonne National Laboratory, 9700 South Cass Ave., Argonne, IL 60439, USA.

[‡] Present address: Center for Exotic Nuclear Studies, Institute for Basic Science (IBS), Daejeon 34126, Korea.

excited states are known, but the spins of most states are not firmly assigned but limited in a probable range [14]. The spin ranges are derived from a ^{192}Os$(d,p)^{193}$Os [15] experiment, and the difference in population between thermal neutron capture [15,16] and average resonance capture experiments [16]. The average resonance neutron capture experiment is assumed to have populated all spin $1/2^-$ and $3/2^-$ states below 1.7 MeV [16]. By elimination, excited states that are not observed in the average resonance neutron capture reaction can be assigned as different from spin $1/2^-$ or $3/2^-$ [16]. Except for the low-lying isomer at 316 keV, assumed to be spin $9/2^-$ [17,18], no lifetimes of excited states in ^{193}Os are known [14].

To measure lifetimes and firmly assign spins of low-lying excited states a thermal neutron capture experiment was performed at the Institut Laue-Langevin (ILL), using a hybrid spectrometer of high-purity germanium (HPGe) clover detectors and LaBr$_3$(Ce) scintillation detectors.

In Sec. II the experimental details and the γ-γ angular correlation and lifetime analysis procedures are described. In Sec. III the experimental results for the individual excited states are presented and discussed. A brief description of the theoretical calculations, the comparison between experiment and theory, and the discussion of ^{193}Os in the context of shape phase transition is given in Sec. IV. Finally, a summary is given in Sec. V.

II. EXPERIMENTAL DETAILS AND DATA ANALYSIS

The experiment was performed at the Institut Laue-Langevin using the Fission Product Prompt Gamma-Ray Spectrometer (FIPPS) [19]. Excited states in ^{193}Os were populated by a ^{192}Os$(n_{\text{th.}},\gamma)^{193}$Os thermal neutron capture reaction [20] with a cross section of 3.19(16)b [21]. The 240 mg target of ^{192}Os powder with 99% enrichment was irradiated for a total of about 9 days. The FIPPS instrument was used in the fast-timing configuration with a central ring of eight identical fourfold segmented high purity germanium (HPGe) clover detectors and sixteen additional LaBr$_3$(Ce) (hereafter LaBr) scintillation detectors, mounted eight each in forward and backward directions, similar to the configuration described in Ref. [22]. Two different LaBr crystal sizes were used in this experiment: eight 1.5 in. × 1.5 in. LaBr crystals and eight 1.5 in. × 2 in. LaBr crystals, both types with identical diameters but different lengths. Clover detectors were surrounded by bismuth germanate (BGO) shields that were not actively used in the analysis, but still provided passive shielding. A standard analog fast-timing setup, as described in Refs. [23,24], utilizing constant fraction discriminators (CFDs) and time-to-amplitude converters (TACs) was used for precise lifetime determination.

Additional measurements were performed to precisely calibrate the γ-γ time walk of the timing system. The decays of ^{152}Eu and ^{187}W provide calibration points in the ranges 40–1408 keV and 72–552 keV, respectively, defining the low-energy region. For the calibration in the high-energy regime the ^{48}Ti$(n_{\text{th.}},\gamma)^{49}$Ti reaction was measured for about 24 h. This reaction provides calibration points in the range 341–6760 keV, while overlapping in the low-energy region with the other calibration measurements.

The experimental data were sorted with a 1.2 μs coincidence window. The data sorting for the lifetime measurement was further restricted by only validating if exactly one clover crystal, two LaBr detectors, and one TAC were observed within the coincidence window. An additional time condition was placed on the TAC information, to remove random coincidences, well outside the time distributions of interest from the data. Further, to reduce the interdetector Compton scattering, coincidences between neighboring LaBr detectors were excluded in the offline analysis. Combined, these restrictions lead to a significant reduction of random and time-correlated background, and improvement of the experimental data. In most cases, lifetime measurements were performed in threefold coincidences, using the high energy resolution of the HPGe clover detectors to precisely select a γ-γ cascade of interest.

Due to the thick 240 mg target, the low-energy efficiency calibration of the available source measurements did not match the osmium data. Significant absorption was observed below ≈300 keV. The relative efficiency at low energy was calibrated using offline data of the β^- decay of ^{193}Os, which has well-known intensities [21], and was combined with the data points of the ^{152}Eu and ^{187}W source measurements above 500 keV.

A. Angular correlations

The γ-γ angular correlation analysis was performed using the procedure introduced in Ref. [25], developed for a spectrometer with a geometry similar to that of the FIPPS instrument. This method is based on a single variable parametrization of all clover crystal positions, using the symmetric properties of the spectrometer of circularly arranged clover detectors around the target position. The parametrization is used for the minimization of a specific γ-γ angular correlation to extract the effective interaction axes of the system for a given energy combination. With the knowledge of the effective interaction axes of the system, the effective interaction angles can be calculated. A measure for the maximum deviation from the effective interaction axes can be used to closely approximate the attenuation of the angular correlation, due to finite detector sizes. All derived quantities are combined in a Monte Carlo simulation to derive the attenuation corrected angular correlation parameters. Following the advice in Ref. [26], a combined probability distribution S^2 is generated from all available statistical information and used for a standard minimization of S^2 vs $\tan^{-1}(\delta)$ to derive the multipole mixing ratio δ information and to perform spin assignments. All information for performing angular correlation analysis is extracted from the experimental data itself and no detailed simulations of the experimental setup are required. An extended description of this approach is given in Ref. [25]. The case for ^{152}Gd, discussed in Ref. [25], was performed within the framework of this work and verifies the applicability of this method for this experiment.

The analysis of γ-γ angular correlations in this work is mostly performed relative to a primary γ-ray transition,

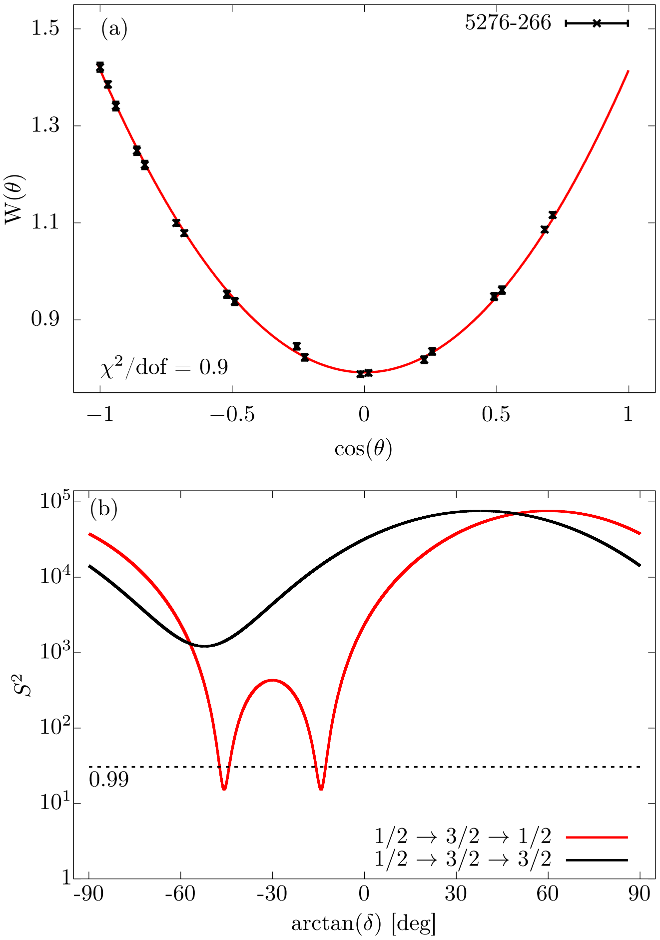

FIG. 1. (a) Angular correlation of the $1/2^+_C \rightarrow 3/2^-_3 \rightarrow 1/2^-_1$ (5276-266 keV) cascade in ^{193}Os. The $1/2^+_C \rightarrow 3/2^-_3$ (5276 keV) primary transition is assumed to be pure $L = 1$ [16]. Effective interaction angles and angular correlation coefficients are derived according to the method outlined in Ref. [25]. The derived attenuation coefficients are $q_2 = 0.979(1)$ and $q_4 = 0.927(3)$ and the extracted final angular correlation coefficients amount to $a_2 = 0.426(4)$ and $a_4 = 0(0)$. (b) Minimization of the mixing ratio δ for different cascades $1/2^+_C \rightarrow 3/2^-_3 \rightarrow J$. The 42 keV state is clearly identified as a spin 1/2 state and the two minima correspond to $\delta_1 = -0.253(7)$ and $\delta_2 = -1.03(2)$ with $S^2_{\text{min}} = 15.4$. The 99% confidence limit [degrees of freedom (dof) = 17] is indicated by the dashed line and results above this limit are rejected.

assumed to be pure $L = 1$ type [16]. With the mixing of one transition assumed to be zero, the mixing ratio of the second γ ray can be determined, and can be used to extract the mixing ratios of further direct coincidences. For γ-γ cascades with spin 1/2 intermediate state the angular correlation is isotropic. For spin 3/2 intermediate states the angular correlation coefficient a_4 is 0, and there exist two mixing ratios δ, minimizing the experimental angular correlation that cannot be differentiated by the a_2 parameter. Further information, e.g., lifetimes, is required to differentiate between these solutions.

In Fig. 1 the analysis of the angular correlation of the $1/2^+_C \rightarrow 3/2^-_3 \rightarrow 1/2^-_1$ (5276-266 keV) cascade is shown as an example. Here, the subscript C denotes the $1/2^+_C$ state as the capture state at 5583 keV, directly populated in the thermal neutron capture reaction. The $1/2^+_C \rightarrow 3/2^-_3$ (5276 keV) transition is one of the strongest primary γ rays observed in this reaction, directly populating the low-lying $3/2^-_3$ (307 keV) state. Due to the spin 3/2 nature of the intermediate 307 keV state, two solutions for the mixing ratio of the $3/2^-_3 \rightarrow 1/2^-_1$ (266 keV) transition are derived. Still, this clean result will be used for the analysis of further transitions feeding the $3/2^-_3$ (307 keV) state, and is essential for the further assignment of spins of excited states.

For γ-γ cascades with both γ-ray transitions mixed, the known mixing ratio of one transition, including its uncertainty, has to be included in the determination of the unknown mixing ratio. This is realized by applying a Monte Carlo approach: a random value from the probability distribution of the known mixing ratios is drawn and a random subset of the measured γ-γ angular correlation is minimized for the unknown mixing ratio. This process is repeated several thousand times to extract the probability distribution of the unknown mixing ratio and corresponding angular correlation coefficients a_k. To improve the precision of a standard minimization algorithm, the general location of the global minimum of the unknown mixing ratio is approximated beforehand by performing a standard S^2 vs $\tan^{-1}(\delta)$ minimization, and used as the starting point for the determination of the unknown mixing ratio. This approach is tested for the $3/2^+ \rightarrow 5/2^+ \rightarrow 3/2^+$ (322-139 keV) cascade in ^{193}Ir, populated in the β^- decay of ^{193}Os. Both mixing ratios are well known with $\delta_{322} = 0.234(10)$ and $\delta_{139} = -0.329(12)$ [14,27]. One literature value is used as input parameter and the second mixing ratio is derived from the experimental data, resulting in $\delta^{\text{expt.}}_{322} = 0.229(15)$ and $\delta^{\text{expt.}}_{139} = -0.322(24)$, in very good agreement with the literature.

This analysis was performed with the in-beam data set, and the direct fit to the angular correlation produced a χ^2/dof significantly larger than 1, and the uncertainties were scaled by $(\chi^2/\text{dof})^{1/2}$, corresponding to the use of the external error. In comparison, the mixing ratios using internal errors amount to $\delta_{\text{expt.}}(322) = 0.229(11)$ and $\delta_{\text{expt.}}(139) = -0.322(17)$. For γ-γ angular correlations with a direct fit with χ^2/dof larger than the rejection limit for the relevant degrees of freedom, external errors are used. This only occurs for γ-γ cascades with the energy of at least one transition below 200 keV and is denoted in the summary of the final results.

The intermediate $5/2^+$ state of the $3/2^+ \rightarrow 5/2^+ \rightarrow 3/2^+$ (322-139 keV) cascade has a lifetime of $\tau = 115(7)$ ps [14], and the possible deorientation of the angular correlation due to the interaction of the intermediate state with extranuclear fields is smaller than the statistical precision [27]. For intermediate states with comparable mean lifetimes, the influence of deorientation effects is assumed to be negligible.

B. Lifetime measurements

Mean lifetimes of nuclear excited states were measured using the generalized centroid difference method (GCD) [23] in combination with fast LaBr scintillation detectors. This well established method is able to precisely measure lifetimes in the range of several pico- to nanoseconds. Only a brief

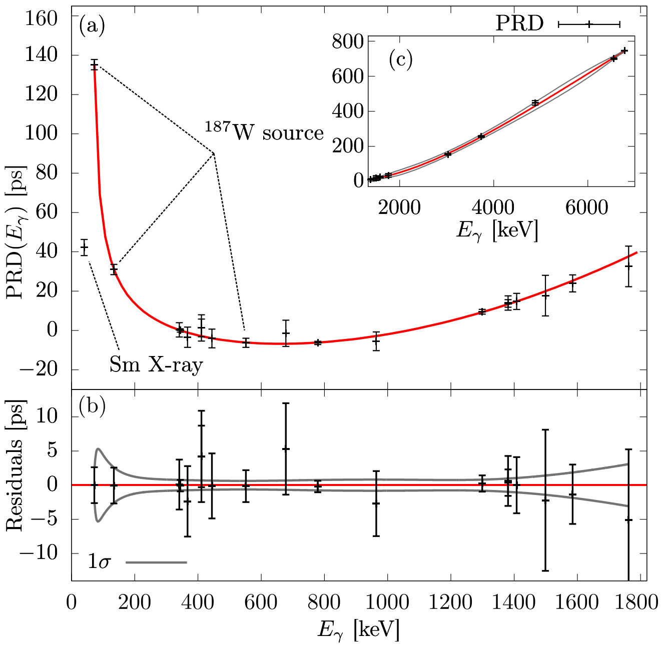

FIG. 2. (a) Combined PRD(E_γ) curve of the experimental setup. The low-energy part is defined by the decays of the ^{152}Eu and ^{187}W sources; the high energy part is calibrated with the ^{48}Ti$(n,\gamma)^{49}$Ti reaction. The 40-1408 keV cascade, emitted following the electron capture (EC) decay of ^{152}Eu, is aligned using the 341-1381 keV cascade in ^{49}Ti. Mean lifetimes used for the calibration are adopted from Refs. [28–31]. (b) Fit residuals of the low-energy PRD(E_γ) curve with the 1σ uncertainty band plotted in gray. The inset (c) shows the separately fitted PRD for the high energy part between 2 and 6.7 MeV, calibrated using the ^{48}Ti$(n,\gamma)^{49}$Ti reaction. For the high-energy PRD, the 3σ standard deviation is adopted as uncertainty, and the corresponding uncertainty band is shown in gray.

summary of the method is presented at this point and a more detailed description of the method is given in Refs. [23,32]. From a conceptual point of view this method is based on measuring the time difference between the γ rays populating and depopulating an excited state of interest and correcting for the combined γ-γ time walk of the measurement devices. Precise time-difference information is measured using constant fraction discriminators and time-to-amplitude converters. Two independent time distributions, the delayed- and antidelayed time distributions, are generated, depending on whether the feeding transitions of the state of interest was observed in a detector connected to the start or stop input of the TAC. By measuring the centroid difference ΔC between the delayed and antidelayed time distributions, and correcting for the prompt response difference (PRD), defining the combined γ-γ time walk of the experimental setup, the mean lifetime of the excited state of interest can be measured directly [23]:

$$2\tau = \Delta C(E_1, E_2) - \mathrm{PRD}(E_1, E_2). \tag{1}$$

The PRD is calibrated by measuring different radioactive sources with precisely known mean lifetimes of excited states. Using the ^{48}Ti$(n_{\mathrm{th.}},\gamma)^{49}$Ti reaction, the PRD is extended up to 6.7 MeV, and the final PRD curve of the experimental setup is shown in Fig. 2. The high energy part of the PRD curve is fitted separately, and the uncertainty of the PRD above 2 MeV is derived from the 3σ standard uncertainty. This careful choice for the uncertainty is based on the observation of slight variations in the determination of the high-energy calibration points, not sufficiently accounted for by the 1σ standard deviation. The low-energy PRD is not affected, and the standard 1σ uncertainty of the fitting procedure is used.

The influence of time-correlated background, directly affecting the measured centroid differences, is analytically corrected by using the standard approach outlined in Ref. [33]. Examples for the analysis procedure and background correction are given in Refs. [34,35].

III. EXPERIMENTAL RESULTS

The aim of this experiment is the investigation of the low-energy negative-parity structure populated in the thermal neutron capture reaction. A partial level scheme is shown in Fig. 3. Lifetime measurements and spin assignments of adopted excited states below 1 MeV were performed using the GCD method and γ-γ angular correlation analysis. In the thermal neutron capture reaction the $1/2^+_C$ capture state at 5583 keV is directly populated, decaying by several primary γ-ray transitions with energies of several MeV, populating specific low-lying excited states [14]. This allows one to precisely select a state of interest for further spectroscopic analysis. From average resonance capture experiments [16] several primary transitions were identified as $E1$ transitions, populating spin $1/2^-, 3/2^-$ states. This information is used to help the spin determination of excited states mostly populated by secondary transitions. If possible, threefold coincidences with one HPGe clover gate on a primary transition are used for the lifetime analysis. This generates almost background free spectra with nearly no contaminations, and allows to precisely measure mean lifetimes of excited states, even in low statistics cases. As example the lifetime measurement procedure is discussed for the 42 keV state, using the 266-42 keV cascade, with a HPGe clover gate placed on the 5276 keV primary transition, directly emitted by the capture state.

The results of the spin assignment performed in this work are combined in Table I, with parities adopted from Ref. [14]. All measured mean lifetimes are combined in Table II. The multipole mixing ratios δ derived in this work are combined in Table III. For several low-lying negative parity states the relative decay intensities were determined and are summarized in Table IV and compared to the recommended values given by the latest ENSDF evaluation [14].

In the following the new experimental results for the individual excited states are discussed, establishing spin assignments and discussing peculiarities of the lifetime measurements.

A. The $1/2^-_1$ state at 41.5 keV

The first excited 42 keV state is assumed to be spin $(1/2^-)$ [14] dominantly populated in a three step cascade following the strong 5276 keV primary γ-ray transitions populating the 307 keV state. From the angular correlation of the 5276-266 cascade shown in Fig. 1 the spin $1/2^-$ assumption can be

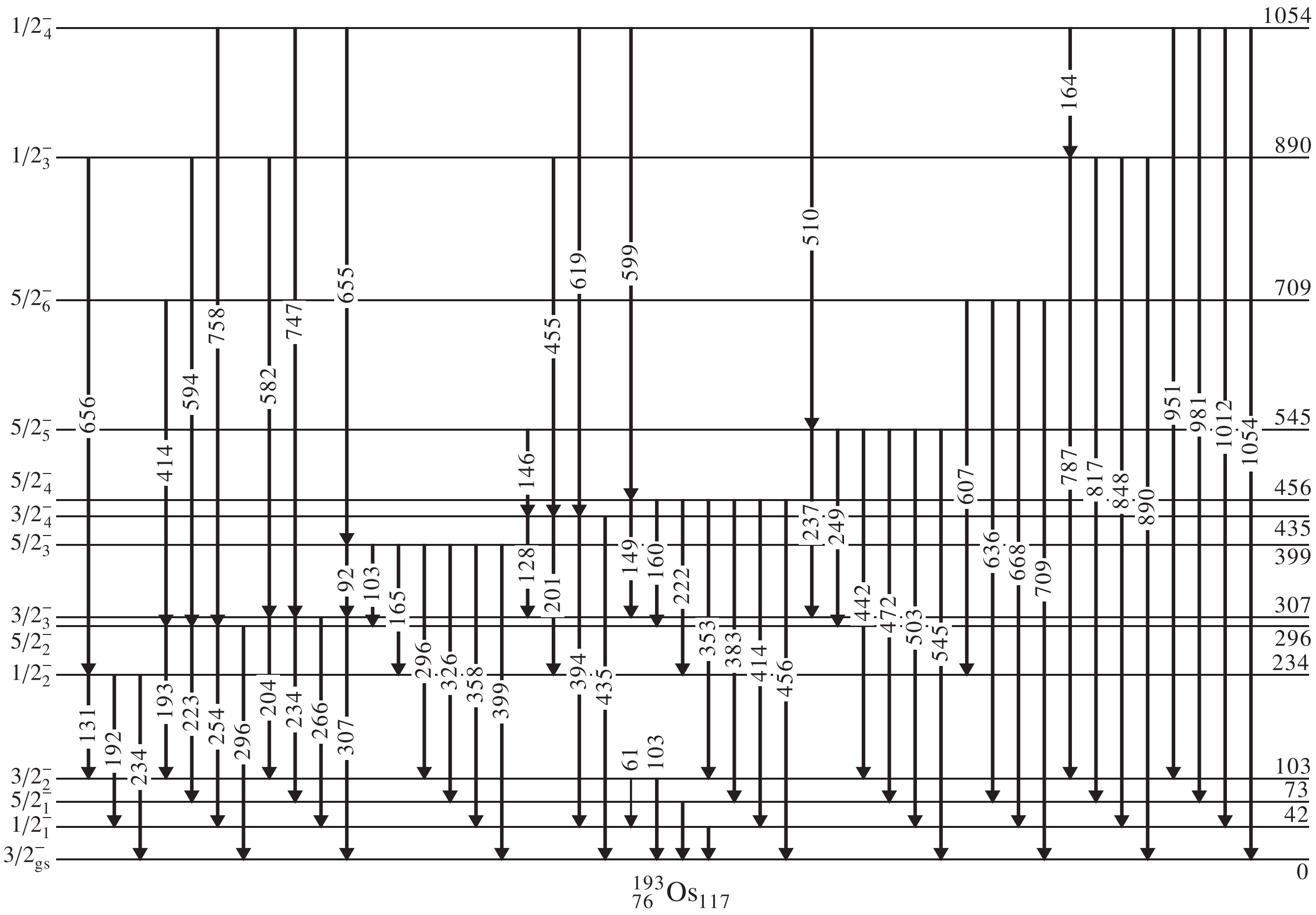

FIG. 3. Partial level scheme of the low-lying negative parity structure in ^{193}Os, investigated in this work. Level and transition energies were adopted from Ref. [14]. Spins of excited states assigned based on Refs. [14,16] and the γ-γ angular correlation analysis performed in this work. The relative γ-ray intensities of the different decay branches are listed in Table IV.

confirmed. The mean lifetime of the 42 keV state can be measured using the 5276-266-42 keV cascade with a HPGe gate placed on the dominant 5276 keV primary transition. The corresponding gated energy spectra are shown in Figs. 4(a) and 4(b). Gating on the 5276 and 266 keV transitions isolates the peak corresponding to the 42 keV ground-state transition. The energy of the 42 keV transition is not sufficient to overcome the binding energy of the K shell electrons and the x-ray peaks at ≈ 60 keV and ≈ 71 keV nearly vanish. The remaining coincident $K\alpha$ and $K\beta$ x rays likely originate from random coincidences and in-target scattering. The time-correlated background beneath the 42 keV peak significantly contributes to the measured centroid difference and is accounted by standard background correction procedure as outlined in Ref. [33]. Due to the low energy of the 42 keV transition, the background beneath the peak is extrapolated from the random background between 80 and 120 keV. Gating on the 5276 and 42 keV transitions completely isolates the peak corresponding to the 266 keV transition as well. The resulting delayed- and antidelayed distributions are shown in Fig. 4(c). From the tailing of the time distributions a comparably long mean lifetime of the 42 keV state is indicated. A precise PRD data point for the 42 keV transition is extracted from the 40 keV x ray emitted directly following the EC decay of ^{152}Eu (see Fig. 2). The final lifetime according to Eq. 1 while accounting for time correlated background [33] amounts to $\tau_{42} = 586(19)$ ps. We note, that a convolution fit

TABLE I. Spins $J^\pi_{\mathrm{expt.}}$ assigned in this work compared to the spins $J^\pi_{\mathrm{lit.}}$ recommended in the latest ENSDF evaluation [14], based on the analysis of the thermal neutron capture and average resonance capture experiments discussed in Ref. [16]. Parities and excitation energies were adopted from Ref. [14].

E (keV)	$J^\pi_{\mathrm{lit.}}$	$J^\pi_{\mathrm{expt.}}$	E (keV)	$J^\pi_{\mathrm{lit.}}$	$J^\pi_{\mathrm{expt.}}$
41.5	$(1/2^-)$	$1/2^{(-)}$	889.5	$1/2^-, 3/2^-$	$1/2^-$
72.9	$(5/2)^-$	$(5/2)^-$	1053.9	$1/2^-, 3/2^-$	$1/2^-$
102.7	$(3/2)^-$	$3/2^-$	1085.4	$(1/2^-, 3/2^-)$	$(3/2^-)$
233.9	$1/2^-, 3/2^-$	$1/2^-$	1170.9	$(1/2^+, 3/2^+)$	$(3/2^+)$
295.7	$(5/2^-)$	$5/2^-$	1178.7	$1/2^-, 3/2^-$	$1/2^-$
307.1	$1/2^-, 3/2^-$	$3/2^-$	1216.9	$1/2^{(-)}, 3/2^{(-)}$	$3/2^{(-)}$
399	$(5/2)^-$	$(5/2)^-$	1281.5	$1/2^-, 3/2^-$	$3/2^-$
435	$1/2^-, 3/2^-$	$3/2^-$	1288.5	$1/2^-, 3/2^-$	$1/2^-$
455.8	$(5/2)^-$	$(5/2)^-$	1386	$1/2^{(-)}, 3/2^{(-)}$	$1/2^{(-)}$
544.6	$(5/2^-, 7/2^-)$	$(5/2^-)$	1515.6	$1/2^-, 3/2^-$	$3/2^-$
709.2	$(5/2^-, 7/2^-)$	$(5/2^-)$	1590.9	$1/2^-, 3/2^-$	$3/2^-$

TABLE II. Results of the lifetime measurements. If multiple cascades were used to derive the mean lifetime, the weighted average with 1σ standard uncertainty is given. Transitions are identified by their energy.

State (keV)	HPGe (keV)	Cascade (keV)	τ (ps)	τ_{adopted} (ps)
$1/2_1^{(-)}$ (41.5)	5276	266-42		586(19)
$3/2_2^-$ (102.7)	5276	204-103	152(12)	150(8)
	4531	951-103	148(11)	
$1/2_2^-$ (233.9)	4225	1126-131		90(8)
$5/2_2^-$ (295.7)	4414	875-254[a]		$100 < \tau < 600$[b]
$3/2_3^-$ (307.1)	3745	1531-266	91(8)	99(6)
	3745	1531-204	103(13)	
	61	5276-204	118(14)	
$(5/2_3^-)$ (399)	4367	819-399		38(10)
$3/2_4^-$ (435)	4531	619-435	17(9)	13(4)
	4531	619-394	11(6)	
	4531	619-201	13(10)	
$(5/2_5^-)$ (544.5)	3980	1059-545		<30
$(5/2_6^-)$ (709.2)	4414	462-709		<23
$1/2_3^-$ (889.5)		4695-890		23(10)
$1/2_4^-$ (1053.9)		4531-951		27(9)

[a] All decay branches including the contamination are included in the gate.

[b] See text for details on the constraints.

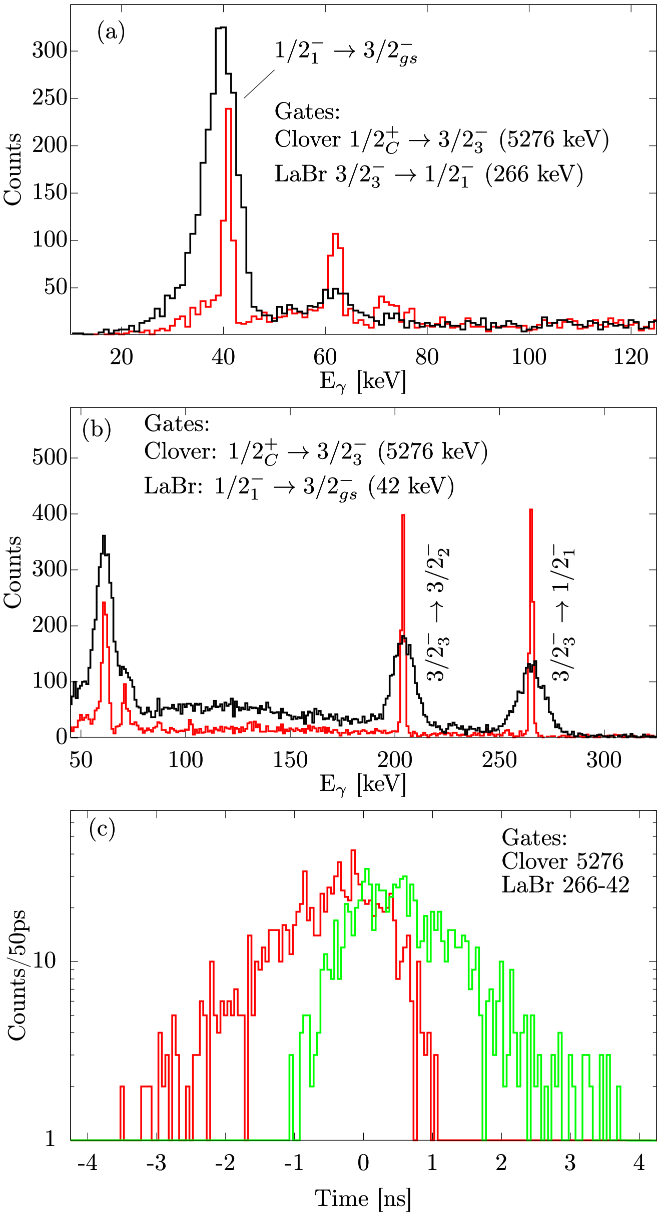

FIG. 4. (a,b) Gated energy spectra used for the lifetime measurement of the $1/2_1^-$ at 42 keV state with the corresponding gates indicated in the figures. The gated LaBr (HPGe) spectrum is shown in black (red) and was generated using HPGe-LaBr-LaBr (HPGe-LaBr-HPGe) threefold coincidences. (a) The energy of the 42 keV transition is not sufficient to overcome the binding energy of the K-shell electrons, and the few visible $K\alpha$ and $K\beta$ x rays originate from random coincidences. (b) The observation of the $3/2_3^- \to 3/2_2^-$ (204 keV) transition in coincidence with the $1/2_1^- \to 3/2_{\text{gs}}^-$ (42 keV) transition indicates the existence of a $3/2_2^- \to 1/2_1^-$ (61 keV) transition. For details see text. (c) Delayed (green) and antidelayed (red) time distributions generated for the $3/2_3^- \to 1/2_1^- \to 3/2_{\text{gs}}^-$ (266-42 keV) cascade. The final resulting mean lifetime after correcting for time-correlated background contributions amounts to $\tau_{42} = 586(19)$ ps.

to the combined statistics of both time distributions yields a mean lifetime of ≈900 ps indicating the non-negligible contribution of time-correlated background, that is not accounted for by the convolution fit.

B. The $(5/2_1^-)$ state at 72.9 keV

The 73 keV state is populated in this experiment and the $(5/2_1^-) \to 3/2_{\text{gs}}^-$ (73 keV) decay transition is visible after gating, e.g., on the $(5/2_2^-) \to (5/2_1^-)$ (223 keV) direct feeding transition. Due to limited statistics lifetime measurements of this state are not feasible

C. The $3/2_2^-$ state at 102.7 keV

The lifetime of the 103 keV state was measured with the 204-103 keV and 951-103 keV cascades, directly populated by the 5276 and 4531 keV primary γ rays, respectively. The resulting mean lifetimes of 152(12) and 148(11) ps agree within their uncertainties.

From the gated spectra shown in Fig. 4(b), with one HPGe gate on the 5276 keV primary γ ray and one LaBr gate on the 42 keV transition a new decay branch of the 103 keV state is hinted. Both the $3/2_3^- \to 1/2_1^-$ (266 keV) and $3/2_3^- \to 3/2_2^-$ (204 keV) transitions are visible. This suggests the existence of a previously unknown $3/2_2^- \to 1/2_1^-$ transition between the 42 and 102.7 keV states with an energy of 61.2 keV. Using HPGe-HPGe-HPGe threefold coincidences, and gating on the 5276 and 42 keV transitions, the efficiency corrected intensity ratio of the 204 and the 266 keV peaks amounts to 0.62(7). In combination with the intensity balance derived for the decay intensities of the 307 keV state this implies that 88(11)% of the 204 keV γ rays emitted from the 307 keV state, end up populating the 42 keV state. This results in relative γ-ray intensities of $I(103\text{ keV}) = 14(13)$ and $I(61.2\text{ keV}) = 100(26)$.

TABLE III. Results of the γ-γ angular correlation analysis and derived mixing ratios. The adopted spin combinations are listed. As noted in Sec. II A, for γ-γ cascades with spin 3/2 intermediate state $a_4 = 0$, and the resulting a_2 value corresponds to two solutions δ_1 and δ_2 for one transition. The mixing ratios δ_1 and δ_2 correspond to the transition marked in bold. Results are ordered relative to the primary transition, emitted from the capture state at 5583 keV, denoted as $1/2^+_C$, and assumed to be pure $L = 1$. The angular correlation parameters $a_{2,4}$ are calculated for the mixing ratios minimizing the measured angular correlation. For details see text.

$J_i \rightarrow J \rightarrow J_f$	Transitions (keV)	Multipolarity	a_2	a_4	δ_1	δ_2
$1/2^+_C \rightarrow 3/2^-_3 \rightarrow 3/2^-_2$	5276-**204**	$E1$-$M1(+E2)$	−0.66(5)	0(0)	−0.170(6)	12.0^{+9}_{-8}
$1/2^+_C \rightarrow 3/2^-_3 \rightarrow 1/2^-_1$	5276-**266**	$E1$-$M1(+E2)$	0.426(4)	0(0)	−0.253(7)	−1.03(2)
$1/2^+_C \rightarrow 3/2^-_3 \rightarrow 3/2^-_{gs}$	5276-**307**	$E1$-$M1(+E2)$	−0.435(7)	0(0)	0.388(18)	1.393(46)
$3/2^-_4 \rightarrow 3/2^-_3 \rightarrow 1/2^-_1$	**128**-266[a]	$M1(+E2)$-$M1(+E2)$	−0.41(3)	0(0)	−0.055(27)	-3.16^{+31}_{-27}
$(5/2^-_4) \rightarrow 3/2^-_3 \rightarrow 1/2^-_1$	**149**-266	$M1(+E2)$-$M1(+E2)$	0.357(24)	0(0)	−0.274(27)	-18^{+5}_{-10}
$(5/2^-_5) \rightarrow 3/2^-_3 \rightarrow 1/2^-_1$	**237**-266	$M1(+E2)$-$M1(+E2)$	0.263(11)	0(0)	−0.176(11)	25^{+9}_{-5}
$1/2^-_3 \rightarrow 3/2^-_3 \rightarrow 1/2^-_1$	**582**-266	$M1(+E2)$-$M1(+E2)$	0.542(18)	0(0)	0.084(14)	1.44(4)
$1/2^-_4 \rightarrow 3/2^-_3 \rightarrow 1/2^-_1$	**747**-266	$M1(+E2)$-$M1(+E2)$	−0.315(14)	0(0)	−0.485(11)	14.5^{+24}_{-16}
$3/2^-_3 \rightarrow 3/2^-_2 \rightarrow 3/2^-_{gs}$	204-**103**[a]	$M1(+E2)$-$M1(+E2)$	0.470(39)	0(0)	0.240(56)	1.89^{+23}_{-21}
$1/2^-_2 \rightarrow 3/2^-_2 \rightarrow 3/2^-_{gs}$	**131**-103[a]	$M1(+E2)$-$M1(+E2)$	−0.425(50)	0(0)	0.047(43)	1.51^{+18}_{-20}
$1/2^-_4 \rightarrow 3/2^-_2 \rightarrow 3/2^-_{gs}$	**951**-103	$M1(+E2)$-$M1(+E2)$	−0.188(17)	0(0)	−0.13(2)	2.42^{+11}_{-13}
$1/2^-_4 \rightarrow 3/2^-_4 \rightarrow 3/2^-_{gs}$	**619**-435	$M1(+E2)$-$M1(+E2)$	−0.85(3)	0(0)	$0.2 < \delta_{1,2} < 1.2$	
$1/2^-_4 \rightarrow 3/2^-_4 \rightarrow 3/2^-_{gs}$	619-**435**	$M1(+E2)$-$M1(+E2)$	−0.85(3)	0(0)	$0.2 < \delta_{1,2} < 1.8$	
$1/2^-_4 \rightarrow 3/2^-_4 \rightarrow 1/2^-_1$	619-**394**	$M1(+E2)$-$M1(+E2)$	0.70(2)	0(0)	$-0.4 < \delta_1 < -0.1$	$-1.3 < \delta_2 < -0.8$
$1/2^+_C \rightarrow 3/2^{(+)} \rightarrow 5/2^-_2$	4414-**875**	$M1$-$E1(+M2)$	0.184^{+31}_{-28}	0(0)	$< -25 \mid > 70$[b]	0.228(56)
$3/2^{(+)} \rightarrow 5/2^-_2 \rightarrow 1/2^-_1$	875-**254**[c]	$E1(+M2)$-$E2(+M3)$	0.103(4)	−0.428(44)	0.005(82)	
$3/2^{(+)} \rightarrow 5/2^-_2 \rightarrow 3/2^-_{gs}$	875-**296**[c]	$E1(+M2)$-$M1(+E2)$	0.157^{+12}_{-21}	0.224^{+63}_{-57}	0.90^{+26}_{-19}	

[a] External errors are used.

[b] Assumed pure $L = 2$ in the following. For details see text.

[c] Effective interaction angles and attenuation coefficients derived for the 582-266 cascade were used for this analysis.

Alternatively, the intensity of the 61.2 keV transition can be derived from the ratios of the $K\alpha_1$ (63 keV), $K\alpha_2$ (61.5 keV), and $K\beta_1$ (73 keV) x-ray peaks. After gating on the $1/2^-_4 \rightarrow 3/2^-_2$ (951 keV) transition, eliminating possible side feeding, the balance of the measured peak volumes $K\alpha_2/K\alpha_1$ significantly increases, while the ratio $K\alpha_1/K\beta_1$ stays the same, indicating a significant contribution of the 61.2 keV γ rays to the combined peak with the 61.5 keV x rays. Using the constant ratio of the emitted x rays, the contribution of the 61.2 keV γ rays to the combined peak can be derived and the intensity ratio with the 103 keV γ ray can be calculated. This results in relative γ-ray intensities of $I(103\text{ keV}) = 9(7)$ and $I(61.2\text{ keV}) = 100(60)$. As outlined above, the efficiency curve in the low-energy region is not well defined, leading to a large uncertainty of the 61.2 keV γ-ray intensity. Still, the results derived using the different approaches are in good agreement with each other, and calculating the weighted average of both results leads to relative γ-ray intensities of $I(61.2\text{ keV}) = 100(24)$ and $I(103\text{ keV}) = 10(6)$.

Taking into account this 61 keV transition and calculating reduced transition strengths in the pure $M1$ and $E2$ limits, yields very large $B(M1)$ and $B(E2)$ values of 0.160(15) and 2500(150) W.u., respectively, for the 61 keV transition. This very large $B(E2)$ value points towards a dominant $M1$ character of this transition. Compared to other transitions observed in this experiment, the resulting $B(M1)$ strengths is enhanced. One possible explanation would be a further unobserved $3/2^-_2 \rightarrow (5/2^-_1)$ (30 keV) transition between the 103 and 73 keV states.

D. The $1/2^-_2$ state at 233.9 keV

Angular correlations with the 234 keV state as intermediate state yield isotropic distributions and spin 1/2 is assigned. The mixing ratio of the strongest 131 keV decay branch is determined from below using the $1/2^-_2 \rightarrow 3/2^-_2 \rightarrow 3/2^-_{gs}$ cascade. Based on the measured mean lifetime, the solution $\delta_2(131) = 1.51(20)$ is rejected, yielding a reduced transition strength larger than 800 W.u.

E. The $5/2^-_2$ state at 295.7 keV

This state is only weakly populated in the (n, γ) reaction with the most intense population stemming from the $1/2^+_C \rightarrow 3/2^{(+)} \rightarrow 5/2^-_2$ (4414-875 keV) cascade. Following the discussion in Ref. [16] and the stated missing observation of the 4414 keV feeding primary transition in the average resonance neutron capture reaction the 1170 keV state is assigned $(1/2^+, 3/2^+)$. With a clearly observable anisotropy of the 4414-875 cascade, shown in Fig. 5(a), the intermediate state can be identified as 3/2. But from this angular correlation it is not conclusive whether the final 296 keV state is $3/2^{(+)}$ or $5/2^{(-)}$. Assuming the primary 4414 keV transition to be pure $L = 1$, the intermediate 875 keV state to be 3/2, and the 296 keV state to be 5/2, the angular correlation yields two solutions for the multipole mixing ratio of the assumed $E1 + M2$ 875 keV transition: $\delta_1(875) = 0.22(6)$ and $\delta_2(875) > 20$. Based on the very strong a4 component of the 875-254 keV angular correlations, shown in Fig. 5(b), with well pronounced anisotropy, the 296 keV state is assigned 5/2, with the 875

TABLE IV. Relative intensities of transition decaying from selected states of the low energy structure of ^{193}Os. Only low-lying negative parity states are taken into account. Relative γ-ray intensities "Int.$_{\text{expt.}}$" are compared to the literature values with "Int.$_{\text{lit.}}$" from Ref. [14]. The reduced transition probabilities $B(M1)$ and $B(E2)$ derived from the measured mean lifetimes are listed and compared to the theoretical calculations in the IBFM-2 framework. For details see text. For $A = 193$, 1 W.u. corresponds to $1.79\mu_N^2$ for $M1$ transitions and to 66.26 $e^2\text{fm}^4$ for $E2$ transitions. Experimental $B(M1)$ and $B(E2)$ values marked with an asterisk ($\ast$) are calculated in the pure $M1$ or $E2$ limit. Note, if angular correlations yielded two solutions for the multipole mixing ratio and no conclusion could be drawn, for comparison reasons, the experimental value with best agreement with the theoretical calculations is shown.

					$B(M1)$ (W.u.)		$B(E2)$ (W.u.)	
State (keV)	E_γ (keV)	J_f	Int.$_{\text{expt.}}$	Int.$_{\text{lit.}}$	Expt.	Theor.	Expt.	Theor.
$1/2_1^-$ (41.5)	41.5	$3/2_{\text{gs}}^-$	100	100	$0.055(2)\ast$	0.065	$694(25)\ast$	60.7
$(5/2_1^-)$ (72.9)	72.9	$3/2_{\text{gs}}^-$	100	100		0.014		8
$3/2_2^-$ (102.7)	102.7	$3/2_{\text{gs}}^-$	100	100	0.030(2)[b]	7.8×10^{-5}	60(30)[b]	12
	102.7	$3/2_{\text{gs}}^-$	[10(6)][a]		0.003(2)[b]	7.8×10^{-5}	6^{+6}_{-4} [b]	12
	[61.2]	$1/2_1^-$	[100(24)][a]		$0.16^{+2}_{-1}\ast$	0.039	$2.5(2) \times 10^3\ast$	2.6
	[29.8]	$5/2_1^-$				0.008		28
$1/2_2^-$ (233.9)	131.2	$3/2_2^-$	100.0(32)	100.0(15)	0.043(4)[b]	0.09	2.3^{+56}_{-20} [b]	5.2
	192.4	$1/2_1^-$	1.2(2)	1.1(2)	$1.6(3) \times 10^{-4}$	0.013		
	233.9	$3/2_{\text{gs}}^-$	2.5(2)	1.7(2)	$1.9(3) \times 10^{-4}\ast$	0.015	$1.3(2)\ast$	11.2
$5/2_2^-$ (295.7)	193	$3/2_2^-$	8.4(13)	11(1)	$2.2(3) \times 10^{-4} < B(M1) < 0.0013(2)\ast$	0.005	$2.5(4) < B(E2) < 15(2)\ast$	28.7
	222.8	$5/2_1^-$	46.3(20)	51.0(14)	$8.0(3) \times 10^{-4} < B(M1) < 0.0048(2)\ast$	1.2×10^{-4}	$6.7(3) < B(E2) < 41(2)\ast$	3.9
	254.2	$1/2_1^-$	100(3)	100.0(19)			$7.5(2) < B(E2) < 45(1)$	16.5
	295.7	$3/2_{\text{gs}}^-$	61.3(21)	64(1)	$2.5(7) \times 10^{-4} < B(M1) < 0.0016(4)$	0.007	$1.0(3) < B(E2) < 6(2)$	3.5
$3/2_3^-$ (307.1)	204.4	$3/2_2^-$	70.0(3)	84.0(16)	$7(1) \times 10^{-5}$ [c]	1.4×10^{-5}	97(6)[c]	17.2
	234.2	$5/2_1^-$	1.81(3)	1.8(1)	$1.8(10) \times 10^{-4}\ast$	0.006	$1.3(7)\ast$	3.4
	265.6	$1/2_1^-$	100.0(4)	100.0(7)	0.0064(4)[b]	0.024	2.3(2)[b]	4.3
	307.1	$3/2_{\text{gs}}^-$	18.9(1)	18.9(4)	$2.8(2) \times 10^{-4}$ [c]	0.02	2.3(2)[c]	3.7
$(5/2_3^-)$ (399)	91.9	$3/2_3^-$	15.5(44)	100(22)	$0.043^{+2}_{-1}\ast$	0.003	$2220^{+940}_{-630}\ast$	2.9
	103.3	$5/2_2^-$	12.8(40)		$0.03(1)\ast$	1×10^{-4}	$1030^{+490}_{-340}\ast$	1.2
	165.2	$1/2_2^-$	11.4(24)	<45			88^{+40}_{-26}	14.1
	296.3	$3/2_2^-$	7.2(25)		$6(3) \times 10^{-4}\ast$	0.066	$3^{+2}_{-1}\ast$	10.9
	326.1	$5/2_1^-$	31.1(40)	89(4)	$0.0020^{+10}_{-5}\ast$	0.0014	$8^{+3}_{-2}\ast$	5.4
	357.5	$1/2_1^-$	5.2(16)	27(4)			0.9^{+4}_{-3}	0.03
	399	$3/2_{\text{gs}}^-$	100(10)	<447	$0.0034^{+14}_{-8}\ast$	0.048	$9^{+4}_{-2}\ast$	12.6
$3/2_4^-$ (435)	127.9	$3/2_3^-$	16.5(10)	20(2)	0.06^{+3}_{-1} [b]	0.0013	4^{+6}_{-3} [b]	7.3
	201.1	$1/2_2^-$	77.0(12)	100(2)	$0.07^{+3}_{-2}\ast$	0.017	$700^{+300}_{-170}\ast$	4.6
	393.5	$1/2_1^-$	100.0(14)	99.0(19)	$0.010^{+4}_{-2} < B(M1) < 0.011^{+5}_{-3}$ [b]	0.025	$0.3(1) < B(E2) < 4^{+2}_{-1}$ [b]	3
	435	$3/2_{\text{gs}}^-$	35.3(8)	43.4(14)	$7^{+3}_{-2} \times 10^{-4} < B(M1) < 0.0030^{+10}_{-5}$	0.003	$0.24^{+10}_{-6} < B(E2) < 5^{+2}_{-1}$	0.3
$(5/2_4^-)$ (455.8)	148.7	$3/2_3^-$	38.2(29)	40.3(25)		0.018		1.8
	160.1	$5/2_2^-$	14.2(18)	14.3(25)		0.04		3.2
	221.9	$1/2_2^-$	8.8(17)	6.7(8)				5.1
	353.1	$3/2_2^-$	24.6(17)	16.8(17)		0.023		0.2
	382.9	$5/2_1^-$	96.0(31)	78.2(25)		0.001		0.05
	414.3	$1/2_1^-$	48.5(21)	38.7(17)				5.2
	455.8	$3/2_{\text{gs}}^-$	100.0(33)	100.0(25)		0.012		1.1
$(5/2_5^-)$ (544.5)	145.5	$(5/2_3^-)$	13.7(24)	23(5)	$>0.013(2)\ast$	0.0047	$>254(41)\ast$	0.8
	237.4	$3/2_3^-$	72.7(34)	83.7(23)	$>0.015(1)$[b]	0.0052	$>3.5(5)$[b]	0.1
	248.8	$5/2_2^-$	23.9(22)	26.7(12)	$>0.0045(4)\ast$	0.0005	$>30(3)\ast$	1.8
	441.8	$3/2_2^-$	25.3(22)	28(5)	$>1.5(7) \times 10^{-4}\ast$	0.0057	$>1.8(2)\ast$	5.8
	471.6	$5/2_1^-$	19.2(29)	26(3)	$>5.0(8) \times 10^{-4}\ast$	1.8×10^{-4}	$>1.0(2)\ast$	0.8
	503	$1/2_1^-$	29.8(22)				$>1.1(1)$	5.0
	544.5	$3/2_{\text{gs}}^-$	100.0(43)	100(3)	$>0.0018(1)\ast$	0.0015	$>2.5(1)\ast$	1.1
$(5/2_6^-)$ (709.2)	413.5	$5/2_2^-$	8.7(7)	10.6(16)	$>1.0(7) \times 10^{-4}\ast$	0.0021	$>2.1(2)\ast$	0.2
	606.5	$3/2_2^-$	23.3(9)	22(2)	$>7.8(3) \times 10^{-4}\ast$	2.7×10^{-4}	$>0.84(3)\ast$	0.3
	636.3	$5/2_1^-$	26.5(10)	33.3(24)	$>7.7(3) \times 10^{-4}\ast$	0.0012	$>0.75(3)\ast$	0.7
	667.7	$1/2_1^-$	20.9(9)				$>0.46(2)$	4.5
	709.2	$3/2_{\text{gs}}^-$	100.0(20)	100(4)	$>0.0021(3)\ast$	0.0064	$>1.64(2)\ast$	0.3

TABLE IV. (*Continued.*)

State (keV)	E_γ (keV)	J_f	Int.$_{\text{expt.}}$	Int.$_{\text{lit.}}$	$B(M1)$ (W.u.) Expt.	$B(M1)$ (W.u.) Theor.	$B(E2)$ (W.u.) Expt.	$B(E2)$ (W.u.) Theor.
$1/2^-_3$ (889.5)	454.5	$3/2^-_4$	4.0(1)		$3^{+2}_{-1} \times 10^{-4}*$	0.0039	$0.5^{+3}_{-1}*$	0.2
	582.4	$3/2^-_3$	21.4(3)	21.7(13)	$6^{+5}_{-2} \times 10^{-4}$ [b]	0.064	$5^{+4}_{-2} \times 10^{-3}$ [b]	1.5
	593.8	$5/2^-_2$	0.42(8)				0.013^{+10}_{-4}	2.7
	655.6	$1/2^-_2$	15.8(2)	19.8(13)	$3^{+2}_{-1} \times 10^{-4}$	0.0013		
	786.8	$3/2^-_2$	67.7(7)	85(3)	$8^{+6}_{-3} \times 10^{-4}*$	0.006	$0.5^{+3}_{-2}*$	4×10^{-4}
	816.6	$5/2^-_1$	14.2(2)	15.3(13)			0.09^{+7}_{-3}	3.0
	848	$1/2^-_1$	6.0(1)		$6^{+4}_{-2} \times 10^{-5}$	7.5×10^{-5}		
	889.5	$3/2^-_{\text{gs}}$	100.0(12)	100(4)	$8^{+6}_{-3} \times 10^{-4}*$	0.014	$0.4^{+3}_{-1}*$	2.1
$1/2^-_4$ (1053.9)	164.4	$1/2^-_3$	0.48(2)	2.8(11)	0.001^{+5}_{-2}	3.9×10^{-4}		
	509.5	$(5/2^-_5)$	0.12(2)				0.011^{+6}_{-3}	6.7
	598.9	$(5/2^-_4)$	0.81(3)				0.04^{+2}_{-1}	0.03
	618.9	$3/2^-_4$	7.5(1)	8.9(4)	$2.0^{+10}_{-5} \times 10^{-4} < B(M1) < 2.6^{+13}_{-6} \times 10^{-4}$	0.001	$0.010^{+5}_{-3} < B(E2) < 0.16^{+8}_{-4}$	2.1
	654.9	$(5/2^-_3)$	0.70(3)				0.02(1)	12.6
	746.8	$3/2^-_3$	8.24(12)	8.7(4)	$1.4^{+7}_{-3} \times 10^{-4}$ [b]	0.022	0.012^{+11}_{-6} [b]	6.9
	758.2	$5/2^-_2$	0.26(3)				0.003^{+2}_{-1}	2.4
	951.2	$3/2^-_2$	100.0(17)	100(6)	$1.4^{+7}_{-4} \times 10^{-4}$ [c]	1.9×10^{-4}	0.4^{+2}_{-1} [c]	9.9
	981	$5/2^-_1$	1.01(2)				0.004^{+2}_{-1}	0.06
	1012.4	$1/2^-_1$	11.7(2)		$1.0^{+5}_{-2} \times 10^{-4}$	0.0024		
	1053.9	$3/2^-_{\text{gs}}$	6.1(1)		$4^{+2}_{-1} \times 10^{-5}*$	6×10^{-5}	$0.015^{+7}_{-4}*$	0.09

[a] Potential second decay branch observed. The transition strengths are calculated once without and once including the second decay branch. For details see text.

[b] Solution δ_1 from Table III used for the calculation of $B(\sigma L)$ values.

[c] Solution δ_2 from Table III used for the calculation of $B(\sigma L)$ values.

keV transition assumed to be pure $L = 2$. A precise lifetime measurement of the 296 keV state is not possible. The state is only weakly populated and all relevant decaying transitions are close in energy, overlapping in the LaBr spectrum, yielding an undefined shape with a total width of about 100 keV. Additionally, all transitions feeding the 296 keV state have a close-lying transition feeding the 307 keV state, since the 12 keV energy difference between such feeding transitions can not be resolved in the LaBr detectors, and a gate on any decaying transitions of the 296 keV state will always include portions decaying from the 307 keV state. Still, we try to give a reasonable estimate, limiting the range of the lifetime of the 296 keV state: from standard analysis procedure, placing a broad gate on the structure including all decaying transitions of the 296 keV state, including all possible contamination, and placing a comparable gate on the, also not well defined, peak of the feeding structure, the mean lifetime after background correction amounts to ≈300 ps. From this, one can safely assume the mean lifetime of the 296 keV to be larger than the lifetime of the 307 keV state, also included in all applied gates. To constrain the upper limit of the lifetime, the shape of the time distribution can be considered: no signs of an exponential slope can be identified. In comparison the time distribution shown in Fig. 4(c), and measured for the 266-42 keV cascade, with the lifetime of the 42 keV intermediate state of 586(19) ps, the beginning of a slope is clearly visible. While at such low energies the shape of the time distribution is usually strongly affected by time-walk effects, the PRD shown in Fig. 2 indicates a low influence for the 266-42 keV cascade, and the mean lifetime of the 296 keV state can be constrained by the mean lifetime of the 42 keV state as an upper limit. This upper limit is chosen cautiously, but from the well defined γ-γ angular correlation shown in Fig. 5(b), one can estimate the mean lifetime to be close to the lower limit of 100 ps.

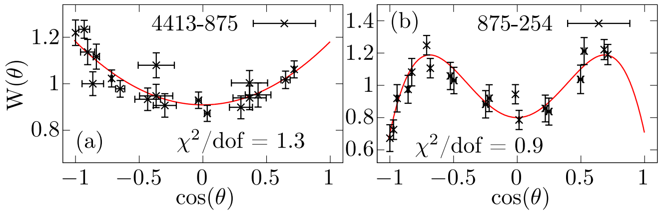

FIG. 5. Angular correlations of the (a) 4414-875 keV and (b) 875-254 keV γ-γ cascades. The distinct shape of the $3/2^{(+)} \rightarrow 5/2^-_2 \rightarrow 1/2^-_1$ (875-254 keV) cascade is only possible for a nearly pure $E2$-$E2$ cascade. From the significant a_4 component the 296 keV state can clearly be assigned as $5/2^-_2$.

F. The $3/2^-_3$ state at 307.1 keV

The 307 keV state is directly populated by the dominant 5276 keV primary transition, allowing for high-precision angular correlation analysis of the decaying 266 keV transition. This transition with defined mixing ratio information is used as a reference transition to derive the mixing ratios for several coincident γ rays and define the spins of the emitting states.

The lifetime of the 307 keV state is measured using three different cascades: two approaches utilize a clover gate on the 3746 keV primary transitions to select the 1531-266/204 cascades, yielding 91(8) and 103(13) ps, respectively. We note the low statistics of ≈ 230 counts (1531-204 keV cascade) and

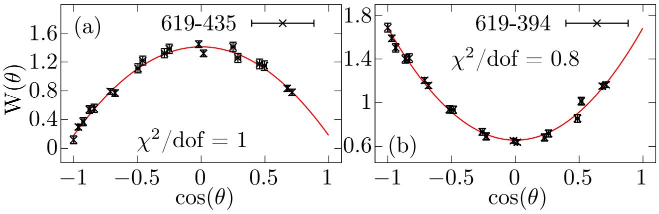

FIG. 6. Angular correlations of the (a) $1/2^-_4 \rightarrow 3/2^-_4 \rightarrow 3/2^-_{\rm gs}$ (619-435 keV) and (b) $1/2^-_4 \rightarrow 3/2^-_4 \rightarrow 1/2^-_1$ (619-394 keV) cascades. A direct fit to the angular correlations yields (a) $a_2 = -0.85(3)$ and (b) $a_2 = 0.70(2)$. The corresponding mixing ratios cannot be precisely determined but only constrained in its range. For details see text.

≈ 340 counts (1531-266 keV cascade) per time distribution. The third approach utilizes the 5276-204 keV cascade with the 5276 keV primary transition directly feeding the 307 keV state. A third gate is placed on the 61 keV peak, assumed to contain the $3/2^-_2 \rightarrow 1/2^-_1$ transition to select the cascade of interest. Indeed, after applying a LaBr gate on the 5276 keV transitions and a HPGe gate on the 61 keV peak, only the 204 keV transition is visible in the corresponding LaBr spectrum, and the measured lifetime amounts to $\tau = 118(14)$ ps.

G. The $(5/2^-_3)$ state at 399 keV

The 399 keV state is only weakly populated in the reaction and the analysis, with about 150 counts per time spectrum, yields a lifetime of $\tau = 38(10)$ ps. In Ref. [16] spin 5/2 is suggested for the 399 keV state. No sufficiently strong cascade for γ-γ angular correlation is available to confirm this spin. Based on the short mean lifetime of the state, and the existence of decaying transitions populating the $1/2^-_1$ and $1/2^-_2$ states, the spin (5/2) assignment is adopted.

H. The $3/2^-_4$ state at 435 keV

The mean lifetime of the 435 keV state was measured using the 619 keV decay of the $1/2^-_4$ state at 1054 keV, directly populated by the 4531 keV primary γ ray, and the three strongest decay transitions of the 435 keV state. All three measured lifetimes are in good agreement, and the weighted average yields $\tau_{435} = 13(4)$ ps.

Angular correlations with the 435 keV as intermediate state are anisotropic and based on Ref. [16] spin $3/2^-$ is assigned. For the solution $\delta_{128} = -3.16$, derived from the $3/2^-_4 \rightarrow 3/2^-_3 \rightarrow 1/2^-_1$ (128-265 keV) angular correlation, the resulting $B(E2)$ strength would be larger than 1600 W.u., and this solution is rejected. Angular correlations with the 435 keV intermediate state are only feasible for the $1/2^-_4 \rightarrow 3/2^-_4$ (619 keV) feeding transition. But this transition decays from 1054 keV spin 1/2 state, and the mixing ratio of this transitions cannot be fixed relative to a well defined primary transition. Still, based on the very large anisotropy of both cascades, shown in Fig. 6, the range of the mixing ratios of several transitions can be constrained. The shape of the $1/2^-_4 \rightarrow 3/2^-_4 \rightarrow 3/2^-_{\rm gs}$ (619-435 keV) angular correlation, with $a_2 = -0.85(3)$, is possible only if both transitions involved in the cascade have a mixing ratio with positive sign. To further restrict the range of the mixing ratios, a uniform random draw of positive mixing ratios for the 619 keV transition is performed and minimized to find the corresponding solutions for the 435 keV transition. Only solutions producing the global $\chi^2_{\rm min}$ are considered further. This constraint reduces the possible solution space to $0.2 < \delta_{619} < 1.2$ and $0.2 < \delta_{435} < 1.8$. These ranges contain two solutions each for the corresponding mixing ratio δ, due to the spin 3/2 nature of the 435 keV state. Applying the solution range of δ_{619} to the $1/2^-_4 \rightarrow 3/2^-_4 \rightarrow 1/2^-_1$ (619-393.5 keV) angular correlation limits the mixing ratio of the 394 keV transition to $-0.4 < \delta_{394} < -0.1$ and $-1.3 < \delta_{394} < -0.8$ with two well separated solutions. Still, this information is not sufficient to further refine the deduced mixing ratios.

I. The $(5/2^-_4)$ state at 455.8 keV

No sufficiently strong feeding transition for lifetime measurements of the 456 keV state could be found. Still, the spin $5/2^-$ assignment of Ref. [16] is preferred by the analysis of the $(5/2^-_4) \rightarrow 3/2^-_3 \rightarrow 1/2^-_1$ angular correlation: assuming the 456 keV state to be 7/2, the resulting mixing ratio δ would imply >30% $M3$ contribution, and spin (5/2) is adopted.

J. The $(5/2^-_5)$ state at 544.5 keV

Due to low population of the 545 keV state the lifetime measurement of this state is hindered. The result of the 1059-545 keV cascade, populated by the 3980 keV primary transition, yields a lifetime of $\tau = 4(13)$ ps. For the second measurement the summed statistics of the 625-545 and 633-545 keV cascades, populated by the 4414 and 4406 keV primary transitions, respectively, are used, and the lifetime amounts to $\tau = 9(10)$ ps. Note the low statistics of $\approx$150 counts and $\approx$250 counts per time spectrum for the first and second analysis, respectively. We adopt an upper limit of <30 ps for the mean lifetime of the 545 keV state, corresponding to roughly 2σ of both results. With the low and widely spread population of the 545 keV state, angular correlation measurements with this state as intermediate are not feasible. Still, the spin of $(5/2^-_5, 7/2^-)$ spin assignment suggested by Ref. [16] can be resolved by analysis of the $(5/2^-_5) \rightarrow 3/2^-_3 \rightarrow 1/2^-_1$ (237-266 keV) cascade: assuming spin $7/2^-$ for the 545 keV state leads to larger 20% $M3$ contribution to the 237 keV transition, and spin $(5/2^-_5)$ is adopted for the 545 keV state.

K. The $(5/2^-_6)$ state at 709.2 keV

The lifetime of the 709 keV state is measured using the $3/2^{(+)} \rightarrow (5/2^-_6) \rightarrow 3/2^-_{\rm gs}$ (462-709 keV) cascade, following the decay of the 4413 keV primary transition, and results in $\tau = 12(11)$ ps, and we adopt an upper limit of $\tau < 23$ ps. Note the low statistics of about 130 counts per time spectrum. In Ref. [16] spin $(5/2^-, 7/2^-)$ is suggested for the 709 keV state, but the angular correlation of the 462-709 keV cascade is nearly anisotropic and no assignment can be made based on the angular correlation analysis. Still, the observation of the previously unknown 668 keV decay transition to the $1/2^-$ (42 keV) state and the short mean lifetime of the 709 keV state suggests the assignment of spin $(5/2^-_6)$.

L. The $1/2_3^-$ state at 889.5 keV

In the literature, the 890 keV state is noted to be a doublet of two close-lying states with energies of 888.6 and 889.5 keV [14]. We observe the excited state directly populated by 4695 keV primary transition to decay with a γ-ray energy of 889.5 keV, and adopt this value for the excitation energy of the state. The $1/2_C^+ \to 1/2_3^- \to 3/2_{\text{gs}}^-$ (4695-890 keV) angular correlation is isotropic and spin $1/2_3^-$ is assigned. Lifetime measurements of this state are only feasible using twofold coincidences with the directly feeding primary transitions, with no other feeding transition strong enough to provide sufficient statistics. This analysis in twofold coincidences results in a mean lifetime of 23(10) ps.

M. The $1/2_4^-$ state at 1053.9 keV

Angular correlations with the 1054 keV states as intermediate state are isotropic and the state is assigned spin $1/2_4^-$. The lifetime measurement in twofold coincidences yields a lifetime of $\tau = 27(9)$ ps.

N. Further spin 1/2, 3/2 states

From the average resonance capture experiment several further states were assigned spin 1/2, 3/2 [16]. For the 1170.9, 1216.9, 1281.5, 1515.6, and 1590.9 keV states clear anisotropy is visible for angular correlations with the primary feeding transition and the strongest decay branch of the state of interest, and spin 3/2 is assigned. For the 1178.7, 1288.5, and 1386 keV states no anisotropy was observed and tentatively spin 1/2 is assigned.

IV. IBFM CALCULATIONS AND DISCUSSION

Theoretical calculations in the framework of the interacting boson-fermion model (IBFM) [36], using constrained self-consistent mean-field calculations as microscopic foundation, are performed. Only a brief description of the methodology is presented, and a detailed discussion is given in Refs. [12,13,37,38]. Deformation energy surfaces, defined by the deformation parameters (β, γ), are calculated for the even-even core within the constrained Gogny-D1M Hartree-Fock-Bogoliubov (HFB) approach [13,39,40]. The Hamiltonian of the IBM-2 is then mapped on the HFB energy surfaces to reproduce the overall pattern in the IBM-2 energy surface [37], and all parameters of the IBM-2 Hamiltonian of the even-even core are derived on the basis of microscopic calculations. Only the boson-fermion coupling is phenomenologically derived by fitting to reproduce the low-lying excitation spectrum of the odd-*A* nucleus [12].

The IBFM-2 Hamiltonian consists of the even-even boson core Hamiltonian $\hat{H}_B$, the fermion single-particle Hamiltonian $\hat{H}_F$ and the boson-fermion interaction Hamiltonian $\hat{H}_{BF}$ [12]:

$$\hat{H}_{\text{IBFM}} = \hat{H}_B + \hat{H}_F + \hat{H}_{BF}. \tag{2}$$

The doubly magic nucleus ^{208}Pb is used as inert core and all valence particles are treated as holes. For the calculation of ^{193}Os, with six valence proton holes and nine valence neutron holes, the nucleus ^{194}Os, with $N_\pi = 3$ and $N_\nu = 4$ bosons, is used as the even-even boson core [13]. As fermion valence space for the remaining neutron hole, the $3p_{1/2}$, $3p_{3/2}$, $2f_{5/2}$, $2f_{7/2}$, and $1h_{9/2}$ orbitals of the neutron major shell $N = 82$–126 are used. The boson-fermion interaction Hamiltonian for nuclei with odd neutron number is defined as [13]

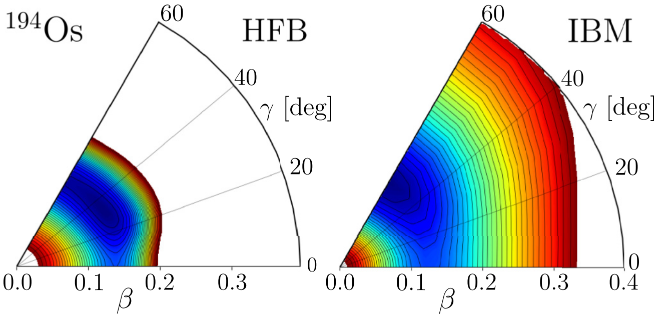

FIG. 7. Potential energy surfaces for the even-even core nucleus ^{194}Os calculated for (left) the Gogny-HFB method and (right) the mapped IBM-2 Hamiltonian. The energy difference between the neighboring contours is 100 keV, with the minimum in blue.

$$\hat{H}_{BF} = \Gamma_\nu \hat{Q}_\pi^{(2)} \cdot \hat{q}_\nu^{(2)} + \Lambda_\nu \hat{V}_{\pi\nu} + A_\nu \hat{n}_{d\nu} \hat{n}_\nu \tag{3}$$

The first term is the quadrupole dynamical term, the second term is the exchange interaction and third term is the monopole interaction. A detailed description of the individual terms is given in Ref. [13]. The coupling parameters Γ_ν, Λ_ν, and A_ν in Eq. (3) are fitted to reproduce the energies of the lowest-lying excited states in ^{193}Os, and are given in Ref. [13].

The potential energy surface (PES) for ^{194}Os in the (β, γ) space, calculated with the microscopic Gogny-D1M HFB approach, is shown in Fig. 7, next to the mapped IBM-2 potential energy surface. Some differences in the PES are visible: while the minima in the β-parameter are located at nearly the same deformation for both the HFB and IBM PES, the IBM surfaces is more shallow and extends further in the β direction, up to $\beta > 0.4$, compared to the steep minimum in the HFB PES. For the γ parameter the minimum in the HFB PES extends from the triaxial deformation at $\gamma \approx 30^\circ$ towards oblate deformation with $\gamma = 60^\circ$. In contrast the minimum in γ in the IBM PES is near the oblate side with the minimum close to $\gamma = 60^\circ$.

A. Energy levels

The excitation energies resulting from the IBFM-2 calculations are compared to the experimental level scheme in Fig. 8. The first nine states up to the $5/2_3^-$ state are in the same order as observed in the experiment. Most other states are in general well reproduced, with some close lying pairs of states swapping their positions. The $9/2_1^-$ state is predicted to be higher in energy, one keV below the $5/2_3^-$ state. The $3/2_4^-$ and $5/2_4^-$ states retain their low energy difference, but their ordering is swapped and moved 300 keV higher. Notably, the $1/2_3^-$ state is the only state significantly breaking with the ordering of states observed in the experiment: the theoretical calculations place the $1/2_3^-$ state 200 keV lower, well below the $5/2_4^-$ state. A general difference in the calculated levels can be observed. While the energies of all spin $1/2^-$ states

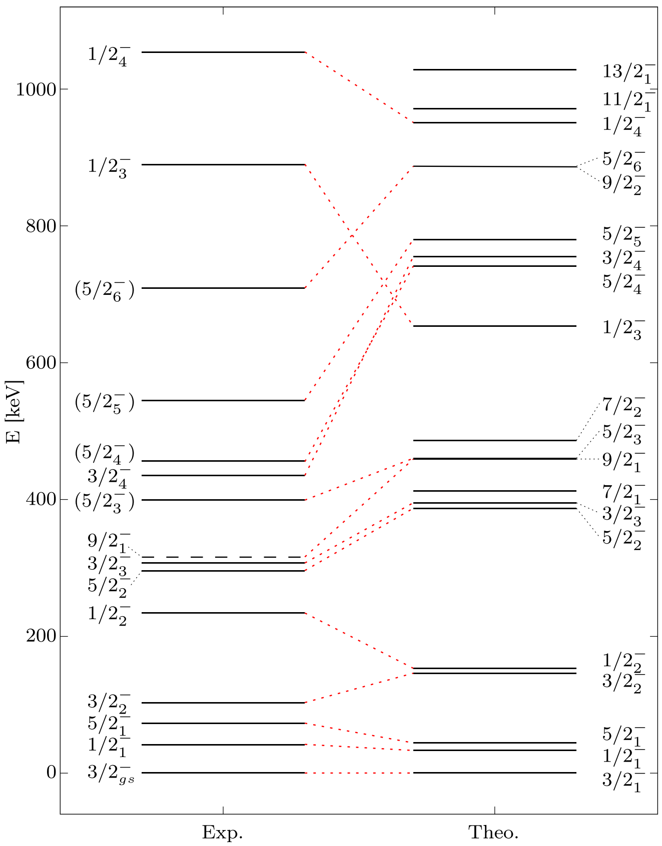

FIG. 8. Comparison of experimental (left) and calculated (right) level scheme of the low-lying negative parity states in ^{193}Os. The corresponding counterparts of the individual experimental and theoretical states are connected by dotted red lines to guide the eye. Experimental energies were adopted from [14].

are underestimated in the theoretical calculations, the energies of all spin $3/2^-$ and $5/2^-$ states above the first three excited states are overestimated.

This overestimation of excitation energies of the $3/2^-$ and $5/2^-$ states above ≈ 200 keV leads to a gap in the theoretical excitation spectrum of about 200 keV, where no further excited states are predicted. In Ref. [13], a similar effect is observed in the calculated excitation spectrum for ^{195}Pt, with the non-yrast states being overestimated in the theoretical calculation, also producing a pronounced gap in the excitation spectrum.

In the relevant energy range the theoretical calculations predict further spin 7/2 and 9/2 states with no known experimental counterpart. Little population of 7/2 and 9/2 states is expected in the thermal neutron capture reaction: The directly populated $1/2^+_C$ capture state dominantly decays in three step cascades towards the ground state.

While the energies of the calculated levels do not fully match the experimental states, the ordering of the calculated levels is in reasonably good agreement with the experiment up to 500 keV.

In Table V the percentage composition values of the IBFM wave function for the $3p_{1/2}$, $3p_{3/2}$, $2f_{5/2}$, $2f_{7/2}$, $1h_{9/2}$ neutron single-particle orbitals are given. The compositions of the $3/2^-_2$ and $1/2^-_2$ and $1/2^-_4$ states have a large overlap in the $3p_{1/2}$, $3p_{3/2}$, and $2f_{5/2}$ orbitals, suggesting similar origin of the states, and one expects dominant transitions between such states.

TABLE V. Fractions of the ($3p_{1/2}$, $3p_{3/2}$, $2f_{5/2}$, $2f_{7/2}$, $1h_{9/2}$) neutron orbital configuration of the corresponding wave function. All values given in percent.

J	$3p_{1/2}$	$3p_{3/2}$	$2f_{5/2}$	$2f_{7/2}$	$1h_{9/2}$
$3/2^-_{\mathrm{gs}}$	26	43	5	25	1
$1/2^-_1$	47	21	9	16	7
$5/2^-_1$	27	5	44	4	20
$3/2^-_2$	1	24	50	12	13
$1/2^-_2$	3	33	39	9	15
$5/2^-_2$	12	32	30	16	9
$3/2^-_3$	13	23	39	9	16
$7/2^-_1$	25	42	5	26	2
$9/2^-_1$	27	6	43	4	21
$5/2^-_3$	3	38	32	17	11
$7/2^-_2$	3	12	59	7	20
$1/2^-_3$	14	30	42	6	7
$5/2^-_4$	18	39	17	20	6
$3/2^-_4$	23	22	30	11	14
$5/2^-_5$	9	21	44	10	17
$9/2^-_2$	8	31	33	15	12
$5/2^-_6$	19	13	46	7	16
$1/2^-_4$	3	34	38	16	10

In Ref. [15], based on observed (d, p) cross section systematics, the $3/2^-_{\mathrm{gs}}$ ground state and the $(5/2^-_1)$ (73 keV) state are proposed to be members of a $3/2^-[512]$ rotational band. Further, both the $1/2^-_1$ (42 keV) and the $3/2^-_2$ (103 keV) states are proposed to be members of the $1/2^-[510]$ rotational band [15]. In contrast, the Coriolis calculations presented in Ref. [16] indicate that the $3/2^-[512]$ and $1/2^-[510]$ orbitals alone cannot contribute sufficient strengths to account for the observed cross sections. The theoretical calculations performed in this work do not support the proposed band structures: little overlap in the orbital fractions (see Table V) is observed for the proposed band member states.

B. Transition strengths

Using the information derived in this work, reduced transition probabilities $B(M1)$ and $B(E2)$ were calculated, and are compared to the predictions of the theoretical model. All values are combined in Table IV. For transitions with no available multipole mixing ratio information, the strengths are calculated in the limit of pure $M1$ and pure $E2$, and are marked with an asterisk. For transitions with multipole mixing ratios derived in this work, the solution used for the calculations of the transition strengths is denoted.

For several states the IBFM calculations yield a satisfactory description, reproducing several structural features of ^{193}Os. The IBFM calculations reproduce the properties of the first excited $1/2^-_1$ (42 keV) state. The theoretical calculations predict a strong $M1$ transition with a small degree of $E2$ contribution. The experimental transition strength in the limit of pure $M1$

is in very good agreement with the theoretical value. The unlikely large $B(E2)$ value in the pure $E2$ limit further suggests the transition to be of dominant $M1$ type. Assuming a 0.6% $E2$ contribution (corresponding to $\delta = 0.075$) reproduces the theoretical $B(E2)$ strengths with the resulting experimental $B(M1) = 0.050(2)$ W.u.

Only the existence of the $5/2_1^-$ state could be confirmed by decays populating this states, but no further experimental information could be derived. The theoretical calculations again suggest a dominant $M1$ transition, and, with the assumption of $\approx$1% $E2$ contribution, a lifetime of $\tau \approx 1.5$ ns would reproduce the theoretical predictions.

For the $3/2_2^-$ state a new decaying transition was observed experimentally, but the corresponding reduced strengths of the new $3/2_2^- \rightarrow 1/2_1^-$ (61 keV) transition are significantly enhanced, compared to other transitions observed in this nuclei. For this reason, the reduced transition strengths were calculated for two situations: once with and once without taking into account the new decaying transition. Neither assumption is quantitatively described by the theoretical calculations. If the $3/2_2^- \rightarrow 3/2_{\mathrm{gs}}^-$ (103 keV) transition is assumed as the only decay branch of the $3/2_2^-$ state, the expected dominant $M1$ character of this transition is not reproduced, underestimating the experimental $B(M1)$ strengths by several orders of magnitude. Taking into account the $3/2_2^- \rightarrow 1/2_1^-$ (61 keV) transition, with the assumption on the intensity balance discussed in Sec. III F, leads to strongly enhanced experimental $M1$ transition strengths, significantly larger than any other other $M1$ strengths observed in this experiment. In this case the theory underestimates the transition strengths, but predicts the $3/2_2^- \rightarrow 1/2_1^-$ (61 keV) transition to be dominantly $M1$, orders of magnitude stronger than the $3/2_2^- \rightarrow 3/2_{\mathrm{gs}}^-$ (103 keV) transition. This theoretical prediction is in good qualitative agreement with the experimental observation. The existence of a $3/2_2^- \rightarrow 5/2_1^-$ (30 keV) transition state could distribute the enhanced strength of the $3/2_2^- \rightarrow 1/2_1^-$ (61 keV) transition on a third decay branch. The theoretical calculations predict $B(E2) = 28$ W.u. and $B(M1) = 0.008$ W.u. for a possible 30 keV transition.

The theoretical calculations significantly overestimate the magnitude of the transition strengths of the $1/2_2^-$ (234 keV) states decay branches. While not being able to reproduce the quantitative characteristics, the theoretical calculations are able to predict the qualitative properties of the 234 keV state to a very high degree. For the low-lying negative parity states investigated in this work, the 234 state is the state with the most well defined decay branch. From the relative decay intensities listed in Table IV the $1/2_2^-$ (234 keV) state dominantly decays via the strong $M1$ $1/2_2^- \rightarrow 3/2_1^-$ (131 keV) transition, with the two competing decay branches with relative intensities of less than 3%. The theoretical calculations exactly predict these characteristics, while overestimating the values of the transitions itself: the $1/2_2^- \rightarrow 3/2_1^-$ (131 keV) transition, calculated to be nearly pure $M1$, is predicted to dominate the decay of the $1/2_2^-$ (234 keV) state. This characteristic is mirrored by the orbital configurations of the two states which show a large overlap (see Table V). The components of the IBFM-2 wave function for the $1/2_2^-$ state are $3p_{1/2}$ (3%), $3p_{3/2}$ (33%), $2f_{5/2}$ (39%), $2f_{7/2}$ (9%), and $1h_{9/2}$ (15%) while the components for the $3/2_2^-$ state are $3p_{1/2}$ (1%), $3p_{3/2}$ (24%), $2f_{5/2}$ (50%), $2f_{7/2}$ (12%), and $1h_{9/2}$ (13%). This large overlap of the wave function might suggest the two states to originate from the same general structure. The theoretical calculations predict the $1/2_2^-$ state at lower excitation energy compared to the experimental value, moving the excited $1/2_2^-$ and $3/2_2^-$ states close together. The resulting underestimated energy of the theoretical $1/2_2^- \rightarrow 3/2_1^-$ transition can explain the overestimation of the predicted transition strength.

Further, while the $1/2_2^-$ and $3/2_2^-$ states show large overlap in the wave function, the $3/2_2^-$ (103 keV) state and the $3/2_{\mathrm{gs}}^-$ ground state, with composition percentages of $3p_{1/2}$ (26%), $3p_{3/2}$ (43%), $2f_{5/2}$ (5%), $2f_{7/2}$ (25%), and $1h_{9/2}$ (1%), show very small overlap of the wave function. This significant difference in the wave function hints a theoretical context for the weak $3/2_2^- \rightarrow 3/2_{\mathrm{gs}}^-$ (103 keV) transition and the preferred, newly observed $3/2_2^- \rightarrow 1/2_1^-$ (61 keV) decay branch, discussed above.

For the higher-lying states the theoretical calculations start to further diverge from the experimental values. For the $5/2_2^-$ and $3/2_3^-$ states some general features observed in the experiment are still reproduced. For example the pure $E2$ $5/2_2^- \rightarrow 1/2_1^-$ transition is well described by the calculations, but, for all other decays of the $5/2_2^-$ state, significant deviation in either the $B(M1)$ or $B(E2)$ strengths are observed. Also for the $3/2_3^-$ state, the $3/2_3^- \rightarrow 3/2_2^-$ transition, with strong $B(E2)$ contribution and hindered $B(M1)$ is qualitatively reproduced, and the $3/2_3^- \rightarrow 1/2_1^-$ transition is in reasonable agreement with the experiment. The $B(M1)$ contributions of further decaying transitions of the $3/2_3^-$ state are significantly overestimated. For the $5/2_3^-$, $3/2_4^-$, $5/2_4^-$, $5/2_5^-$, $1/2_3^-$, $1/2_4^-$, and $5/2_6^-$ states the experimental transition strengths are not satisfyingly reproduced and, any possible accordance with the experimental values appears to be random. From the comparison of excitation energies shown in Fig. 8, the increasing deviation between experimental and theoretical levels already builds the expectation of the properties of the higher energetic states to no longer agreeing with the experiment. This deviation might be explained by the single-particle energies and occupation probabilities of the odd nucleon not being a sufficiently realistic approximation to reproduce the extended level structure [13]. This is due to difficulties in deriving the coupling parameters κ for nuclei close to $N = 126$ [7,8]. It might be interesting to investigate if there is a systematic for which type of states the excitation energies are increased or decreased. In the present case, all spin $1/2^-$ states above 200 keV are systematically lowered while the $3/2^-$ and $5/2^-$ states are raised in energy.

C. Discussion

It is important to again emphasize that the theoretical predictions are based on the results of the constrained HFB calculations, which are used as microscopic foundation to define the characteristics of the IBM-2 Hamiltonian for the even-even nucleus ^{194}Os [13,37]. Only the coupling constants of the boson-fermion interaction are phenomenologically derived by fitting to experimental low-lying states of the odd-A nuclei [12]. From this point of view, the predictions of the theoretical calculations for the spectroscopic properties of the low-lying structure in ^{193}Os are reasonably good up to an energy of 500 keV.

The calculated Gogny-D1M HFB deformation energy surfaces for the even-even osmium isotopes suggest a gradual change from prolate to oblate-soft shape, indicating a prolate-to-oblate shape phase transition occurring in the even-even osmium isotopes between ^{192}Os and ^{194}Os [13]. A change in shape is also suggested by the trend of the energies of the excited 2_2^+ and 0_2^+ states for the osmium isotopes. The energies of the 2_2^+ states continuously decrease for $^{188-192}$Os and start rising again for ^{194}Os. For the 0_2^+ states the energies stay in the same order for $^{188-192}$Os but suddenly drop by 300 keV for ^{194}Os, indicating a change happening in the underlying structure [41–44].

Significant structural changes are also observed in the neighboring odd-A osmium isotopes. The ground state of ^{191}Os changes from spin $9/2^-$ to $3/2^-$ for ^{193}Os, accompanied by a reordering of the low-spin states. Further, calculated effective deformation parameters $\beta_{\mathrm{eff.}}$ and $\gamma_{\mathrm{eff.}}$ abruptly change going from ^{189}Os towards ^{193}Os, serving as indicator for a shape phase transition [13]. The PES of ^{194}Os used for the definition of the IBM-2 Hamiltonian parameters, shown in Fig. 7, has a well pronounced oblate minimum with some γ softness. In comparison, the minimum of the HFB PES is located at $\gamma = 30^\circ$, extending towards the oblate side. This implies a bias of a more oblate even-even core used for the IBFM calculations than predicted by the HFB calculations. Still, the Hamiltonian with oblate bias is able to reasonably well reproduce the characteristics of the low-lying structure in ^{193}Os. In combination with the systematic studies in Ref. [13], this carefully points towards the conclusion that the shape of the nucleus ^{193}Os is closer to the oblate deformed shape suggested for ^{194}Os, compared to the shape of the other neighboring nucleus ^{192}Os. This is in agreement with the hypothesis of a rapid shape phase transition occurring in the osmium isotopes with an already oblate ^{193}Os, and the $N = 116$ nucleus ^{192}Os as a transitional nucleus.

V. SUMMARY

A $^{192}\mathrm{Os}(n_{\mathrm{th.}}, \gamma)\,^{193}\mathrm{Os}$ experiment was performed at the ILL, using the FIPPS instrument in the fast-timing configuration to investigate the low-lying negative-parity structure in ^{193}Os. Mean lifetimes of eight excited states in ^{193}Os were measured for the first time, and limits on the lifetime of three further states are established. Using γ-γ angular correlations, the spins of several previously known states were assigned, and the multipole mixing ratios for several transitions were precisely determined. Theoretical calculations in the framework of the IBFM, based on constrained self-consistent mean-field calculations, were performed and compared to the experimentally derived spectroscopic information. The structural properties of the first six excited states are, except for their excitation energies, reasonably well reproduced. Based on the IBM PES with minimum located well on the oblate side, and the satisfactory prediction of the low-lying negative parity structure, the ^{193}Os nucleus is indicated to be oblate deformed. This supports the assumption of a rapid shape phase transition to occur in the osmium isotopes, with ^{192}Os as a transitional nucleus and ^{193}Os and ^{194}Os presumed to be oblate deformed.

ACKNOWLEDGMENTS

Y.H.K. acknowledges support from the Institute for Basic Science (IBS-R031-D1). J.-M.R. and M.L. acknowledge the Deutsche Forschungsgemeinschaft, Germany for support under Grant No. JO 391/18-1.

---

[1] R. Casten, A. Namenson, W. Davidson, D. Warner, and H. Borner, Phys. Lett. B **76**, 280 (1978).

[2] Z. Podolyák, S. J. Steer, S. Pietri, F. R. Xu, H. L. Liu, P. H. Regan, D. Rudolph, A. B. Garnsworthy, R. Hoischen, M. Górska, J. Gerl, H. J. Wollersheim, T. Kurtukian-Nieto, G. Benzoni, T. Shizuma, F. Becker, P. Bednarczyk, L. Caceres, P. Doornenbal, H. Geissel *et al.*, Phys. Rev. C **79**, 031305 (2009).

[3] J. A. Cizewski, R. F. Casten, G. J. Smith, M. L. Stelts, W. R. Kane, H. G. Börner, and W. F. Davidson, Phys. Rev. Lett. **40**, 167 (1978).

[4] A. Ansari, Phys. Rev. C **33**, 321 (1986).

[5] C. Baktash, J. X. Saladin, J. J. O'Brien, and J. G. Alessi, Phys. Rev. C **22**, 2383 (1980).

[6] P. Sarriguren, R. Rodríguez-Guzmán, and L. M. Robledo, Phys. Rev. C **77**, 064322 (2008).

[7] K. Nomura, T. Otsuka, R. Rodríguez-Guzmán, L. M. Robledo, and P. Sarriguren, Phys. Rev. C **83**, 014309 (2011).

[8] K. Nomura, T. Otsuka, R. Rodríguez-Guzmán, L. M. Robledo, and P. Sarriguren, Phys. Rev. C **84**, 054316 (2011).

[9] C. Wheldon, J. Garcés Narro, C. J. Pearson, P. H. Regan, Z. Podolyák, D. D. Warner, P. Fallon, A. O. Macchiavelli, and M. Cromaz, Phys. Rev. C **63**, 011304(R) (2000).

[10] P. R. John, V. Modamio, J. J. Valiente-Dobón, D. Mengoni, S. Lunardi, T. R. Rodríguez, D. Bazzacco, A. Gadea, C. Wheldon, T. Alexander, G. de Angelis, N. Ashwood, M. Barr, G. Benzoni, B. Birkenbach, P. G. Bizzeti, A. M. Bizzeti-Sona, S. Bottoni, M. Bowry, A. Bracco *et al.*, Phys. Rev. C **90**, 021301 (2014).

[11] K. Nomura, T. Otsuka, R. Rodríguez-Guzmán, L. M. Robledo, P. Sarriguren, P. H. Regan, P. D. Stevenson, and Z. Podolyák, Phys. Rev. C **83**, 054303 (2011).

[12] K. Nomura, T. Nikšić, and D. Vretenar, Phys. Rev. C **93**, 054305 (2016).

[13] K. Nomura, R. Rodríguez-Guzmán, and L. M. Robledo, Phys. Rev. C **97**, 064314 (2018).

[14] M. Shamsuzzoha Basunia, Nucl. Data Sheets **143**, 1 (2017).

[15] D. Benson Jr., P. Kleinheinz, R. K. Sheline, and E. B. Shera, Z. Phys. A **285**, 405 (1978).

[16] D. Warner, W. Davidson, H. Börner, R. Casten, and A. Namenson, Nucl. Phys. A **316**, 13 (1979).

[17] S. J. Steer, Z. Podolyák, S. Pietri, M. Górska, H. Grawe, K. H. Maier, P. H. Regan, D. Rudolph, A. B. Garnsworthy, R. Hoischen, J. Gerl, H. J. Wollersheim, F. Becker, P. Bednarczyk, L. Cáceres, P. Doornenbal, H. Geissel, J. Grębosz, A. Kelic, I. Kojouharov *et al.*, Phys. Rev. C **84**, 044313 (2011).

[18] B.-S. Gao, Z. Xiao-Hong, F. Yong-De, Z. Yu-Hu, L. Min-Liang, W. Si-Cheng, W. Jian-Guo, M. Fei, G. Ying-Xiang, W. Xiao-Guang, H. Chuang-Ye, Z. Yun, W. Zhi-Min, Y. Xin-Liang, W. Zhi-Gang, and F. Fang, Chin. Phys. C **38**, 064001 (2014).

[19] C. Michelagnoli, A. Blanc, E. Ruiz-Martinez, A. Chebboubi, H. Faust, E. Froidefond, G. Kessedjian, M. Jentschel, U. Köster, P. Mutti, and G. Simpson, EPJ Web Conf. **193**, 04009 (2018).

[20] L. Knafla, F. Dunkel, A. Esmaylzadeh, J. Garbe, L. M. Gerhard, G. Häfner, J. Jolie, V. Karayonchev, M. Ley, C. Michelagnoli, J.-M. Régis, and K. Schomacker, Institut Laue-Langevin (2020), doi: 10.5291/ILL-DATA.3-17-49.

[21] K. S. Krane, Phys. Rev. C **85**, 044319 (2012).

[22] C. M. Petrache, J.-M. Régis, C. Andreoiu, M. Spieker, C. Michelagnoli, P. E. Garrett, A. Astier, E. Dupont, F. Garcia, S. Guo, G. Häfner, J. Jolie, F. Kandzia, V. Karayonchev, Y.-H. Kim, L. Knafla, U. Köster, B. F. Lv, N. Marginean, C. Mihai *et al.*, Phys. Rev. C **99**, 024303 (2019).

[23] J.-M. Régis, H. Mach, G. Simpson, J. Jolie, G. Pascovici, N. Saed-Samii, N. Warr, A. Bruce, J. Degenkolb, L. Fraile, C. Fransen, D. Ghita, S. Kisyov, U. Koester, A. Korgul, S. Lalkovski, N. Marginean, P. Mutti, B. Olaizola, Z. Podolyak *et al.*, Nucl. Instrum. Methods Phys. Res., Sect. A **726**, 191 (2013).

[24] J.-M. Régis, G. Simpson, A. Blanc, G. de France, M. Jentschel, U. Köster, P. Mutti, V. Paziy, N. Saed-Samii, T. Soldner, C. Ur, W. Urban, A. Bruce, F. Drouet, L. Fraile, S. Ilieva, J. Jolie, W. Korten, T. Kröll, S. Lalkovski *et al.*, Nucl. Instrum. Methods Phys. Res., Sect. A **763**, 210 (2014).

[25] L. Knafla, A. Esmaylzadeh, A. Harter, J. Jolie, U. Köster, M. Ley, C. Michelagnoli, and J.-M. Régis, Nucl. Instrum. Methods Phys. Res., Sect. A **1042**, 167463 (2022).

[26] S. Robinson, Nucl. Instrum. Methods Phys. Res., Sect. A **292**, 386 (1990).

[27] H. Ghaleb and K. Krane, Nucl. Phys. A **426**, 20 (1984).

[28] L. Knafla, A. Harter, M. Ley, A. Esmaylzadeh, J.-M. Régis, D. Bittner, A. Blazhev, F. von Spee, and J. Jolie, Nucl. Instrum. Methods Phys. Res., Sect. A **1052**, 168279 (2023).

[29] T. Burrows, Nucl. Data Sheets **109**, 1879 (2008).

[30] M. Martin, Nucl. Data Sheets **114**, 1497 (2013).

[31] M. Basunia, Nucl. Data Sheets **110**, 999 (2009).

[32] J.-M. Régis, N. Saed-Samii, M. Rudigier, S. Ansari, M. Dannhoff, A. Esmaylzadeh, C. Fransen, R.-B. Gerst, J. Jolie, V. Karayonchev, C. Müller-Gatermann, and S. Stegemann, Nucl. Instrum. Methods Phys. Res., Sect. A **823**, 72 (2016).

[33] J.-M. Régis, A. Esmaylzadeh, J. Jolie, V. Karayonchev, L. Knafla, U. Köster, Y. Kim, and E. Strub, Nucl. Instrum. Methods Phys. Res., Sect. A **955**, 163258 (2020).

[34] L. Knafla, P. Alexa, U. Köster, G. Thiamova, J.-M. Régis, J. Jolie, A. Blanc, A. M. Bruce, A. Esmaylzadeh, L. M. Fraile, G. de France, G. Häfner, S. Ilieva, M. Jentschel, V. Karayonchev, W. Korten, T. Kröll, S. Lalkovski, S. Leoni, H. Mach *et al.*, Phys. Rev. C **102**, 054322 (2020).

[35] L. Knafla, G. Häfner, J. Jolie, J.-M. Régis, V. Karayonchev, A. Blazhev, A. Esmaylzadeh, C. Fransen, A. Goldkuhle, S. Herb, C. Müller-Gatermann, N. Warr, and K. O. Zell, Phys. Rev. C **102**, 044310 (2020).

[36] F. Iachello and O. Scholten, Phys. Rev. Lett. **43**, 679 (1979).

[37] K. Nomura, N. Shimizu, and T. Otsuka, Phys. Rev. Lett. **101**, 142501 (2008).

[38] K. Nomura, N. Shimizu, and T. Otsuka, Phys. Rev. C **81**, 044307 (2010).

[39] S. Goriely, S. Hilaire, M. Girod, and S. Péru, Phys. Rev. Lett. **102**, 242501 (2009).

[40] J. Decharge, M. Girod, and D. Gogny, Phys. Lett. B **55**, 361 (1975).

[41] F. Kondev, S. Juutinen, and D. Hartley, Nucl. Data Sheets **150**, 1 (2018).

[42] B. Singh and J. Chen, Nucl. Data Sheets **169**, 1 (2020).

[43] C. M. Baglin, Nucl. Data Sheets **113**, 1871 (2012).

[44] J. Chen and B. Singh, Nucl. Data Sheets **177**, 1 (2021).